Simulation of oxygen vacancy induced phenomena in ferroelectric thin films

Kwok Tung Li[a) and Veng Cheong Lo
Department of Applied Physics, The Hong Kong Polytechnic University, Hong Kong, China

The role of oxygen vacancy in lead–titanate–zirconate ferroelectric thin film has been numerically simulated using the two-dimensional four-state Potts model. On one hand, the presence of an oxygen vacancy in a perovskite cell strongly influences the displacement of the Ti^{4+} ion. Hence the vacancy–dipole coupling must be considered in the switching mechanism. On the other hand, a space charge layer is established by the inhomogeneous distribution of oxygen vacancies through trapping charge carriers. Consequently, the thickness dependence of the coercive field and remanent polarization are reproduced in the presence of this oxygen vacancy distribution. Frequency, temperature, and driving voltage-dependent polarization fatigue behaviors are also simulated. © *2005 American Institute of Physics.* [DOI: 10.1063/1.1846947]

I. INTRODUCTION

Due to the recent progress of the formation of quality ferroelectric thin films in nanometer scale, these films are now widely used in microelectronic devices because of their capabilities in high speed, small profile, and light weight.[1] On the other hand, the physical properties for thin films are completely distinct from their bulk counterpart. In particular, the dielectric permittivity, remanent polarization, and coercive field vary with film thickness.[2,3] It is imperative to have precise control on these physical properties, especially when the film thickness is small. Developing a better thin film deposition technique is on one side. Pursuing a better understanding on these thickness effects is on the other.

This issue of thickness dependence has been pursued continuously by both experimental investigations and theoretical modelings. Most theories suggested the increasing importance of electrode/film interface when the thickness is small. The nature of this interface is another important issue. Tagenstev *et al.*[4] suggested the screening effect of the external electric field by the injected charge at the surface layer. This layer was considered to be dielectric without spontaneous polarization. Larsen *et al.*[5] proposed the formation of "blocking layer" by the accumulation of oxygen vacancies after the electrode deposition. Again, this "blocking layer" was considered to be nonferroelectric. However, the assumption on the presence of this dead layer has been opposed by Jin and Zhu[6] and Sinnamon *et al.*[7] They argued that there is no experimental evidence for the dead layer. Moreover, experiment has shown that ferroelectricity can still exist in the film of a few nanometers thick.[8] Thus, the assumption of a nonferroelectric interfacial is problematic. In our previous work,[9] instead of assuming a nonferroelectric layer, we proposed that this layer is still ferroelectric with parameters different from those of the interior region. This difference is attributed to the difference in tetragonality at the interfacial layer due to the in-plane stress.

The roles of oxygen vacancy in a perovskite cell are two-fold: modifying the switching behavior of a dipole in a cell and screening the external electric field. The accumulation of oxygen vacancies near the surface creates distinct ferroelectric behavior, resulting in thickness effects. Ma *et al.*[10] correlated this accumulation in the lead-rich surface layer with the enhancement of a coercive field from a $PbTiO_3$ thin film grown on $SrTiO_3$ substrates. Tagantsev *et al.*[11] compared the thickness dependence of the coercive field between Pt/PZT/Pt and RuO_2/PZT/RuO_2 systems. The expected thickness dependence was observed in the first system, but disappeared in the second one. Even though numerous experimental accounts on the role of oxygen vacancies in thickness dependence appear in the literature, a theoretical explanation is still rare.

Polarization fatigue is one of the degradation problems where the switchable polarization is reduced after a number of switching cycles.[12–15] It is also revealed in some fatigue experiments that the coercive field is enhanced.[12] The fatigue behavior has been attributed to the presence of space charge as well as oxygen vacancies in literature.[13] Law *et al.*[16] related the increase in fatigue-free cycles with the increase of oxygen partial pressure during the formation of the RuO_x electrodes. Obviously, increasing the oxygen composition near the electrode leads to the reduction of oxygen vacancies that ultimately enhances the fatigue resistance. Scott *et al.*[17] observed the reduction of the oxygen composition near the electrodes after fatigue, reflecting an increase in oxygen vacancies. Domain wall pinning has been suggested as the way to cause polarization fatigue by oxygen vacancies. Park *et al.*[15] have simulated the pinning effect of oxygen vacancy from the first-principles calculation. Lixin *et al.*[18] concluded that domain-wall pinning is not possible when the vacancy concentration is low.

In this article, we propose that the increase in oxygen vacancies leads to both a reduction in remanent polarization and an enhancement of the coercive field. Furthermore, the trapping and detrapping of charge carriers by vacancies governs the temporal evolution of space charge, leading to the

---

[a)Corresponding author. Electronic mail: 02900440r@polyu.edu.hk

97, 034107-1

© 2005 American Institute of Physics

switching cycle-dependent space charge distribution. The detailed charge trapping mechanism, together with the temperature, frequency, and driving voltage-dependent fatigue behaviors will be presented in Sec. III.

II. THEORY

The q-state Potts model is a generalization of the Ising model with q metastable states. In this study, the four-state ($q=4$) Potts model was adopted. Experiments have observed the coexistence of both 90° and 180° domain walls in perovskite-type thin ferroelectric films,[19] even in single crystalline samples. Thus, it is reasonable to consider that there are four different dipole orientations, mutually perpendicular to each other. In fact, the four-state Potts model has been used to simulate ferroelectric properties previously. For example, Qian et $al.$[20] have investigated the dielectric breakdown in PMN-PT film using this approach.

For a three-dimensional perovskite cell with the elongated edge along the z direction, Ti^{4+} is located inside the cell and there are six faces: top, bottom, left, right, front, and back. The center of each of these faces accommodates one oxygen atom. There are six possible directions for the displacement of Ti^{4+}, each of which is perpendicular to one of these six faces, giving rise to six possible dipole orientations. For the investigation of the thickness effect, the transverse dimension of the film is usually much larger than its thickness. It is assumed that all physical properties only vary along the thickness direction while remaining uniform over the transverse direction. Any effect taking place along the front or back direction is similar to that along the left or right

direction. Consequently, it is adequate to represent the tetragonal cell by a two-dimensional rectangle lying in the x-z plane, and to keep only four states for the dipole orientations. An oxygen vacancy is formed by the removal of an oxygen ion from any center of the six faces of the perovskite cell. By the same token, only those located at the top, bottom, and right edges of a rectangle are included in our model.

The ferroelectric thin film can be represented by a two-dimensional array of rectangles $N_x \times N_z$, where N_x and N_Z are numbers of rectangles along x (transverse) and z (thickness) directions, respectively. A monolayer is a layer having a thickness equal to the elongated edge of a tetragonal preovskite cell, Δz. The thickness of the film is thus related by $d = N_Z \Delta z$ and the width $w = N_x \Delta z$. The location of a rectangle in the film can be described by a pair of indices $((i,j))$, where $0 < i \leqslant N_x$ and $0 < j \leqslant N_Z$. Each rectangle contains a dipole with the orientation denoted by a state variable called pseudospin matrix $\hat{S}_{i,j}$. There are four different states defined as follows:

$$\hat{S}_A = \begin{bmatrix} 1 \\ 0 \end{bmatrix} \text{(upward)}, \quad \hat{S}_B = \begin{bmatrix} 0 \\ 1 \end{bmatrix} \text{(left)},$$

$$\hat{S}_C = \begin{bmatrix} -1 \\ 0 \end{bmatrix} \text{(downward)} \quad \text{and} \quad \hat{S}_D = \begin{bmatrix} 0 \\ -1 \end{bmatrix} \text{(right)}. \quad (1)$$

For a film of infinite transverse size and a finite thickness along the z direction, a periodic boundary condition is adopted at the transverse edges, and free boundary condition at the top and bottom electrodes, as follows:

$$\hat{S}_{0,j} = \hat{S}_{N_x,j}, \quad \hat{S}_{N_x+1,j} = \hat{S}_{1,j}, \quad \text{(Periodic boundary condition along the transverse direction)}; \quad (2)$$

$$\hat{S}_{i,0} = \hat{S}_{i,N_z+1} = \begin{bmatrix} 0 \\ 0 \end{bmatrix}, \quad \text{(free boundary condition along the top and bottom electrodes)}. \quad (3)$$

The initial spin configuration of the film is set to the unpoled condition in the following way. The average domain size, D, is related to the sample size by

$$D = c \times \sqrt{N_Z}, \quad (4)$$

where c is a constant. This relation has been confirmed by experiment.[21] A number of seed dipoles, N_D, are then randomly allocated in the film, where

$$N_D = \frac{N_Z}{c \times \sqrt{N_Z}} = c' \times \sqrt{N_Z}. \quad (5)$$

The state of each allocated seed dipole is also randomly assigned to one of the four states. After the assignment of states for all these seed dipoles, domains are formed by aligning the unassigned cells neighboring the assigned cells

with the same state. The growth proceeds until the states of all rectangles have been assigned.

In the q-state Potts model, the Hamiltonian[22] of the interacting spins is generally expressed as

$$H = -\sum_{i,j} J(\theta_{i,j}), \quad (6)$$

where $J(\theta_{i,j})$ is the coupling function, $\theta_{i,j} = \theta_{n_i} - \theta_{n_j}$ the angle between two spins of states n_i and n_j, $\theta_n = 2\pi n/q$, and $n < q-1$. Wu[22] has discussed the two different ways of expressing the coupling coefficient in the Potts model: the standard Potts model and the planar Potts model. The first model is applicable over all ranges of q while the second one is valid only for $q \leqslant 4$. Moreover, these two models are equivalent for $q=2, 3,$ and 4.

In our present case with $q=4$, we have used the planar

Potts model for simplicity. The possible orientations for each of the spin are: $\theta_n = 0$, $\pi/2$, π, and $3\pi/4$ for $n = 0$, 1, 2, and 3, respectively. The coupling function $J(\theta_{i,j})$ returns the following values:[22] $J(\theta_{i,j}) = \varepsilon_1 \cos(\theta_{i,j}) = \varepsilon_1$ if two spins are parallel, $-\varepsilon_1$ if they are antiparallel, and 0 if they are perpendicular. We can replace this description by the product of two neighboring pseudospin matrices $\{\hat{S}_{i,j}^T \hat{S}_{k,m}\}$, where $\hat{S}_{i,j}^T$ represents the transpose matrix of $\hat{S}_{i,j}$. This product returns the value $+1$ when the two neighboring spins are parallel, -1 when they are antiparallel, and 0 when they are perpendicular. The system Hamiltonian is then given by

$$H_0 = -\sum_{i,j,k,m} J_j \{\hat{S}_{i,j}^T \hat{S}_{k,m}\} - \sum_{i,j} p_{0j} \{\hat{E}_j^T \hat{S}_{i,j}\}, \qquad (7)$$

where J_j is the coupling coefficient between neighboring dipoles and p_{0j} the magnitude of the dipole moment of a cell in the jth layer. For simplicity, only nearest neighbor interactions are included. $\hat{E}_j$ is the electric field in matrix form and its transpose is $\hat{E}_j^T$. In particular, if only an external driving field exists along the z direction, $\hat{E}_j$ is given by

$$\hat{E}_j = \begin{bmatrix} E_Z \\ 0 \end{bmatrix}. \qquad (8)$$

The second term in Eq. (7) represents the coupling between the dipole and the electric field, $\hat{E}_j$, returning the value of $+E_Z$ for a pseudospin along the $+z$ direction, $-E_Z$ for the $-z$ direction, and zero otherwise.

The presence of an oxygen vacancy in a rectangle located at the (i,j) position can also be represented by another matrix $\hat{V}_{i,j}$, with the following values for different positions of the rectangle:

$$\hat{V}_{i,j} = \begin{cases} \begin{bmatrix} 0 \\ 0 \end{bmatrix} \text{ (vacancy is absent),} & \begin{bmatrix} 1 \\ 0 \end{bmatrix} \text{ (at the top plane),} \\ \begin{bmatrix} 0 \\ 1 \end{bmatrix} \text{ (at the left plane),} & \begin{bmatrix} -1 \\ 0 \end{bmatrix} \text{ (at the bottom plane),} \\ \begin{bmatrix} 0 \\ -1 \end{bmatrix} \text{ (at the right plane).} \end{cases} \qquad (9)$$

Oxygen vacancies generated from outside diffuse into the film through the electrodes. The distribution of oxygen vacancies across the thickness of the film can be expressed by the following function:

$$f(z) = \frac{[\exp(-z/L_{z1}) + \exp(-(d-z)/L_{Z2})]}{L_{Z1}[1 - \exp(-d/L_{Z1})] + L_{Z2}[1 - \exp(-d/L_{Z2})]}, \qquad (10)$$

where L_{z1} and L_{z2} are the characteristic diffusion lengths at the top and bottom electrodes, respectively. This function is normalized such that $\int_0^d f(z)dz = 1$, ensuring the same quantity of oxygen vacancies for different L_{z1} or L_{z2} values. For uniform distribution along the z direction, $f(z) \to 1/d$ as $L_{z1} = L_{z2} \to \infty$. On the other hand, the distribution is homogeneous along the transverse direction. The total amount of oxygen vacancies in the film is denoted by N_V. The quantity across a transverse monolayer at a distance z from the top surface is given by $n(z) = N_V f(z)$. The number of oxygen vacancies per unit area is $C_v(z) = (N_V/w)f(z)$. The number of rectangles in the film per unit area is $C_c = (1/\Delta z^2)$. The probability that a oxygen exists in a particular rectangle at the (x, z) position is then related by $P_v(z) = C_v(z)/C_c = (N_V/w)f(z)\Delta z^2$.

For an unstrained rectangle with the elongated edge along the z direction, only two off-center equilibrium positions above and below the center of the rectangle exist. In the absence of oxygen vacancy, Ti^{4+} can be located at one of these equilibrium positions with equal probability. The potential profile along the z axis is symmetric.[23] If the elongated edge is along the x axis, then these two equilibrium positions are located at the left or right of the center. Rectangles inside the domain wall are strained with four equilibrium positions: above, below, and at the left and the right of the center. In the presence of an oxygen vacancy at the top edge of the rectangle, because of the imbalance in Coulombic interactions between ions and the distortion of the perovskite cell, the potential energy for the Ti^{4+} ion is lowest at the bottom equilibrium position. Correspondingly, the potential energy at the top equilibrium position must be highest.[23] The potential energies for the other two equilibrium positions are
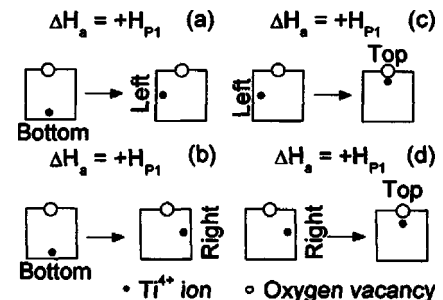

FIG. 1. In the presence of the oxygen vacancy at the top plane, an additional energy H_{P1} is required to displace the Ti^{4+} ion from and to the following equilibrium positions: (a) from the bottom to left; (b) bottom to right; (c) left to top; and (d) right to top.

intermediate. An additional energy, say $2H_{P1}$, is required to displace Ti^{4+} ion from the bottom equilibrium position to the top one. This comprises a 180° switching. Conversely, the same amount of energy is released through the reverse displacement. For a 90° switching, the Ti^{4+} ion at the bottom equilibrium position displaces to either the left or right equilibrium position. It demands an amount of energy H_{P1} for this displacement. For an unstrained rectangle deep inside the domain, there are only two equilibrium positions on opposite sides of the center, only 180° dipole switching can take place. Rectangles inside the 90° domain wall are highly strained that four off-center equilibrium positions exist, enabling 90° dipole switching. It has been shown that 90° switching is dominant because it expends less energy. The energy exchanges through 90° dipole switching are summarized in Fig. 1.

The switching directions of the dipole can be opposite to those shown in Fig. 1, with energy exchanges equal in magnitude but opposite in sign. Moreover, the position of the oxygen vacancy can be at other positions of the rectangle. The same relative position of the Ti^{4+} ion with respect to the oxygen vacancy results in the same potential energy. The Hamiltonian of the system can be expressed by the following expansion:

$$H = H_0 + \sum_{i,j} H_{P1}\{\hat{V}_{i,j}^T \hat{S}_{i,j}\} - H_{P2} \sum_{i,j,k,m} \{\hat{V}_{i,j}^T \hat{V}_{i,j}\}\{\hat{S}_{i,j}^T \hat{S}_{k,m}\},$$
(11)

where H_0 is the Hamiltonian in the absence of oxygen vacancies, the second term on the right-hand side of Eq. (11) is the contribution from the coupling of oxygen vacancies with pseudospins. The presence of an oxygen vacancy induces distortion to the perovskite cell. This distortion influences the coupling with the neighboring dipoles, as manifested in the third term.

The polarization switching is implemented by the conventional Metropolis algorithm. At each Monte Carlo step, a pseudospin in the film is randomly chosen for a trial rotation. This trial is accepted by satisfying the following conditions: (1) $\Delta H < 0$ or (2) $r < \exp(-\Delta H/kT)$, where ΔH is the change in Hamiltonian through the rotation of the selected pseudospin, k is the Boltzmann constant, T is the temperature, and r is a random number in the interval (0, 1). The ensemble of pseudospins of the system is then updated. The polarization can then be calculated by

$$p_Z = \frac{\sum_{i,j} \{\hat{S}_{i,j}^T \times \hat{n}\}}{N_X N_Z},$$
(12)

where $\hat{n}$ is the unit matrix given by $\hat{n} = \begin{pmatrix} 0 \\ 1 \end{pmatrix}$.

The above Monte Carlo algorithm does not shown any time variable, neither implicitly nor explicitly. In order to simulate a time-dependent process, the number of computational steps must be scaled with some characterization time of the system. Considering an initially unpoled system subject to a positive dc field, dipoles inside the film rotate sequentially. The overall polarization gradually increases until it finally attains a steady-state value. The switching time τ is then defined as the time required to arrive 99% of the steady-state value. Both experiments and theory suggest that this time is independent of the system size.[18,19] In our simulation, the switching time, expressed in terms of number of MCS, varies with thickness N_Z according to the following relation:

$$\tau_{MCS} = c_1 \times (N_Z)^{C_2}\omega,$$
(13)

where $c_1 = 24\,796$ and $c_2 = 0.947$ are fitting constants, and ω is a characteristic time step. The subscript "MCS" denotes the number of MCS. Consequently, every physical time must be scaled by the factor τ_{MCS}/τ. For example, the externally applied sinusoidal field can be converted into

$$E = E_m \sin\left(\frac{2\pi t}{\Gamma}\right) = E_m \sin\left(\frac{2\pi t_{MCS}}{\Gamma_{MCS}}\right),$$
(14)

where t is the time and Γ the period. Both of them are physical times. These are converted into $t_{MCS} = t \times (\tau_{MCS}/\tau)$ and $\Gamma_{MCS} = \Gamma \times (\tau_{MCS}/\tau)$, respectively.

Another role of oxygen vacancies is to trap charge carriers, usually holes.[24] They then become space charge. Under thermal equilibrium, the portion of charged vacancies N_V^+ depends on both the position of Fermi level E_F and temperature T, by the following relation:[25]

$$N_V = N_V^X + N_V^+,$$
(15)

where

$$N_V^+ = \frac{N_V}{1 + g_A \exp\left(\dfrac{E_F - E_T}{kT}\right)},$$
(16)

N_V is the total number of vacancies, N_V^X is the uncharged portion, and E_T is the energy of the trapping level above the valence band. The space charge density ρ_{SC} is then related to N_V^+ by

$$\rho_{SC} = \frac{qN_V^+}{w\Delta z}f(z) = q_r f(z).$$
(17)

The parameter q_r depends not only on the position of the Fermi level and temperature, but also on the imbalance of trapping and emission rates of charge carriers and the frequency of the alternating driving field. The space-charge-induced local field E_{SC} can then be obtained from the Poisson equation,

$$\frac{dE_{SC}}{dz} = \frac{1}{\varepsilon_S \varepsilon_0}\rho_{SC}.$$
(18)

If the explicit form of the distribution function is given, the analytical form for E_{SC} can be derived.

The above variables are converted into dimensionless forms by the following relations:

$$h = H/J_B, \quad h_{P1} = H_{P1}/J_B, \quad h_{P2} = H_{P2}/J_B,$$

$$e_Z = E \times p_0^B/J_B, \quad \hat{e} = \begin{bmatrix} e_z \\ 0 \end{bmatrix}, \quad t_e = kT/J_B,$$

$$\tilde{z} = z/\Delta z, \quad N_{Z1} = L_{Z1}/\Delta z, \quad N_{Z2} = L_{Z2}/\Delta z,$$
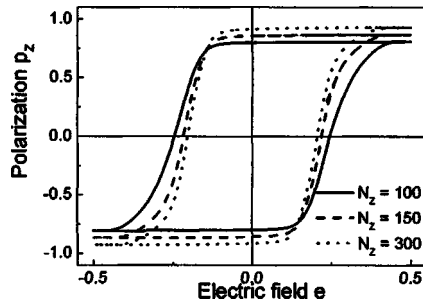
FIG. 2. Hysteresis loops for difference thickness: $N_Z=100$ (solid), $N_Z=150$ (dashed), $N_Z=300$ (dotted).

FIG. 3. Thickness dependence of coercive field e_c for a different amount of oxygen vacancies N_V.

$$\tilde{q}_r = \frac{p_0 q N_V^+}{J_B \varepsilon_S \varepsilon_0 N_X \Delta z^2}, \quad e_{SC}(\tilde{z}) = \tilde{q}_r \int_0^{\tilde{z}} f(\tilde{z}')d\tilde{z}', \qquad (19)$$

and

$$\tilde{f}(\tilde{z})$$
$$= \frac{\exp(-\tilde{z}/N_{Z1}) + \exp(-(N_z - \tilde{z})/N_{Z2})}{N_{Z1}[(1 - \exp(-N_Z/N_{Z1})] + N_{Z2}[1 - \exp(-N_Z/N_{Z2})]}.$$

The electric field, contributed by both the external driving field and the space-charge-induced local field, can be expressed in the following matrix form:

$$\hat{e} = \begin{bmatrix} e_{\text{ext}} + e_{SC} \\ 0 \end{bmatrix}. \qquad (20)$$

After the conversion, the normalized Hamiltonian now becomes

$$h = -\sum_{i,j,k,m} \{\hat{S}_{i,j}^T \hat{S}_{k,m}\} - \sum_{i,j} \{\hat{e}_j^T \hat{S}_{i,j}\} + h_{P1}\sum_{i,j} \{\hat{V}_{i,j}^T \hat{S}_{i,j}\}$$
$$- h_{P2}\sum_{i,j,k,m} \{\hat{V}_{i,j}^T \hat{V}_{i,j}\}\{\hat{S}_{i,j}^T \hat{S}_{k,m}\}. \qquad (21)$$

III. RESULTS AND DISCUSSION

The validity of our present model has been tested by investigating the effects of the temperature, frequency, and amplitude of the driving electric field. The simulation result shows that the coercive field E_C increases on increasing either the frequency or amplitude of the electric field, but decreases when temperature is increased. All of these results agree with experiments.[26,27]

We have adopted the following numerical parameters: $d=40$ nm, $w=820$ nm, $E_m=2500$ kV/cm, $p_0^B=3.2x10^{-29}$ cm, $\Delta z=0.4$ nm, $T=300$ K, $\Gamma=10$ μs, $N_V=60\,000$, $J_B=0.032$ eV, $h_{P1}=0.064$ eV, $h_{P2}=1.92$ eV, $L_{Z1}=L_{Z2}=12$ nm. These values yield a saturation polarization $P_S=49$ μC/cm^2, which is typical for PZT samples. Moreover, the charge separation between Ti^{4+} and O^{2-} that induces a dipole moment p_B^0 is 0.05 nm, which is comparable to the value 0.063 nm suggested by Joan and Shirane.[28]

The resultant Polarization-Electric (PE) hysteresis loops for different thickness are shown in Fig. 2. The corresponding thickness dependence on the coercive field for a different amount of oxygen vacancies is shown in Fig. 3. It reveals that the coercive field monotonically decreases on increasing
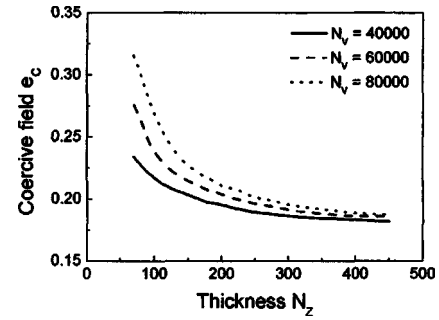
thickness until it approaches an asymptotic value for large N_Z. The thickness dependence of remanent polarization p_r is shown in Fig. 4. As expected, it increases with thickness. The presence of oxygen vacancies reduces the remanent polarization.

We have fitted the experimental results of Fujisawa *et al.*[29] using our present model, as shown in Fig. 5 and Fig. 6 for the coercive field and the remanent polarization. The fitting agrees with the experimental data quite well, except for a slight deviation at small thickness. The coercive field E_C is usually obtained from dividing the coercive voltage V_C by the thickness d, so that $E_C=V_C/d$. For small thickness, a significant error in ΔE_C results because the relative error in thickness measurement $\Delta d/d$ leads to the relative error in the coercive field through the relation $\Delta E_C/E_C \sim \Delta d/d$.

In polarization fatigue, the switchable polarization is reduced as the number of switching cycles N increases. It is caused by the increase in space charge. The oxygen vacancy is a hole trapper.[24,30] It traps a hole when the position of the Fermi level is below the trapping level and releases the hole when the Fermi level is above. The trapping and detrapping of the hole by a neutral species is expressed by the following reaction:

$$V^X + h^+ \Leftrightarrow V^+, \qquad (22)$$

where V^x and V^+ are the vacancy in neutral and singly charged states, respectively. h^+ is a hole. The population of V^+ is governed by Eq. (15).

An alternating driving voltage in the form of a sequence of square pulses with a period Γ is applied to the sample. The pulse width is exactly one-half of the period. Initially, all
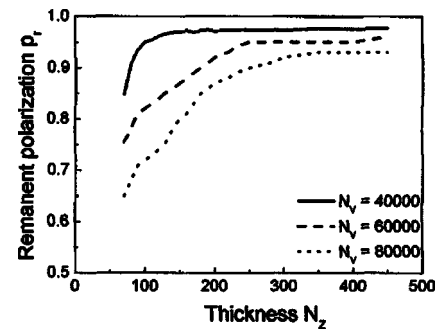

FIG. 4. Thickness dependence of remanent polarization p_r for a different amount of oxygen vacancies N_V.
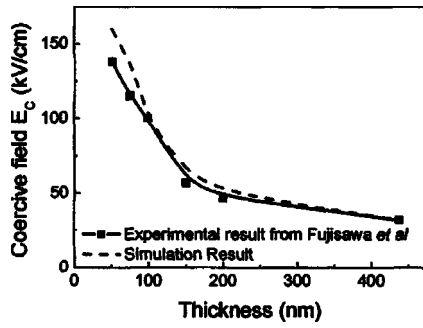
FIG. 5. Thickness dependence of coercive field E_C from (i) the experimental result of Fujisawa (see Ref. 29) (solid line) and (ii) our simulation result (dashed line).

vacancies are in a neutral charge state (untrapped), and $N_V^+ = 0$. The rate of increases for N_V^+ is governed by the following relation:

$$\frac{dN_V^+}{dt} = \sigma_t(N_V - N_V^+) - e_t N_V^+, \tag{23}$$

where σ_t and e_t are, respectively, the capture and emission rates of the holes by oxygen vacancy. During the application of the filling pulse, hole trapping takes place. The first term of Eq. (23) dominates, and the second term is ignored for simplicity. At the end of the filling pulse, the gain in charged vacancies is given by

$$N_V^+ = N_V\{1 - \exp(-\sigma_t\Gamma/2)\} + N_V^+(0)\exp(-\sigma_t\Gamma/2), \tag{24}$$

where $N_V^+(0)$ is the initial number of oxygen vacancies in a positively charged state. At the second half of a cycle, part of the holes is released from the traps, as described by

$$\frac{dN_V^+}{dt} = -e_t N_V^+. \tag{25}$$

For a complete cycle, if the trapping rate is larger than the detrapping one, there must be a gain of charged oxygen vacancies. For instance, after the first cycle, the population of charged oxygen vacancies becomes
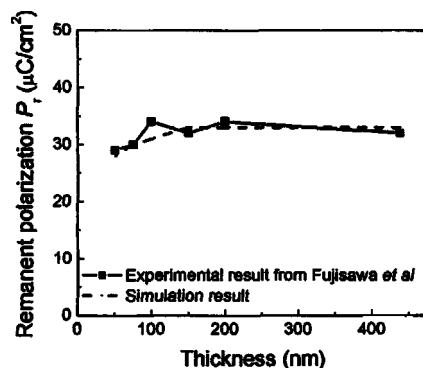

FIG. 6. Thickness dependence of remanent polarization P_r from (i) the experimental result from Fujisawa (see Ref. 29) (solid line) and (ii) our simulation result (dashed line).
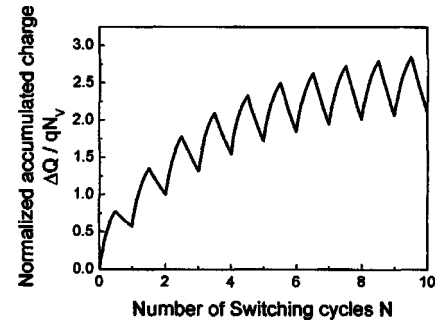

FIG. 7. The plot of accumulated charge $\Delta Q/qN_V$ against the number of switching cycles N ($\Gamma = 300$, $\sigma_t = 0.01$, $e_t = 0.022$).

$$N_V^+(1) = \{N_V[1 - \exp(-\sigma_t\Gamma/2)] + N_V^+(0)\exp(-\sigma_t\Gamma/2)\}\exp(-e_t\Gamma/2) > N_V^+(0), \tag{26}$$

where "(1)" denotes the first cycle. After a number of repetitive pulses, the gain in this charged species is denoted by $N_V^+(N)$. The increase in space charge is $\Delta Q = qN_V^+(N)$. The relation between ΔQ and the number of switching cycles is shown in Fig. 7. The asymptotic behavior of ΔQ for large N has been fitted by the following relation: $\Delta Q = qc_3 N^{0.25}/f$, where $f = 1/\Gamma$ is the frequency of the driving voltage. From Eq. (17), the space charge density can be expressed as follows:

$$\rho_{SC} = \frac{qc_3 N^{0.25}}{N_X(\Delta z)^2 f} f(z). \tag{27}$$

It clearly demonstrates that the space charge density increases with the number of switching cycles. This is the primary cause for polarization fatigue.

We have simulated the effects of temperature, amplitude of the driving voltage, and frequency on polarization fatigue. The effect of temperature obtained both from our simulation (curves) and the experimental result of Paton et al.[31] (symbols) are shown in Fig. 8. At 200 K, both theory and experiment agree quite well. They deviate from each other at 300 and 500 K. This deviation might be due to the omission of the temperature dependence of the population of charged vacancies. Moreover, the trapping and detrapping rate of holes by these vacancies are also temperature dependence, which has been omitted in our present model. Nevertheless, the experimentally observed temperature effect has been qualita-
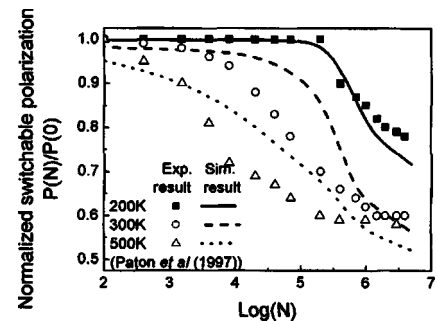

FIG. 8. The effect of temperature on polarization fatigue: curves: simulated results; symbols: experimental result from Paton et al. (see Ref. 31).
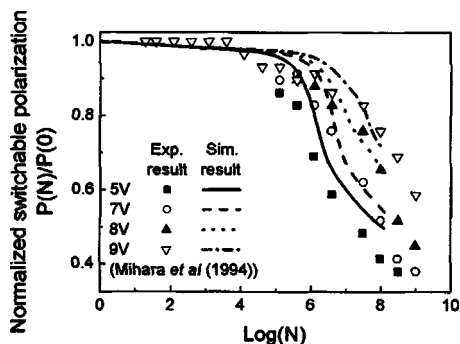
FIG. 9. The effect of amplitude of driving voltage on polarization fatigue: curves: simulation result; symbols: experimental result from Mihara *et al.* (see Ref. 26).

tively reproduced, i.e., the larger the ambient temperature, the faster decay of remanent polarization occurs.

The effect of the amplitude of the driving voltage is shown in Fig. 9, with symbols representing the experimental result of Mihara *et al.*[26] and curves denoting our simulated result. The agreement between experiment and theory is quite well. It is envisaged that the polarization decays faster for a smaller amplitude. In the presence of oxygen vacancies, an additional energy is expensed to switch the dipole in favor of the driving voltage. A low driving voltage does not acquire enough energy to switch the dipole and the portion of unswitchable dipoles increases.

The frequency dependence of polarization fatigue is shown in Fig. 10, with symbols representing the experimental result from Majumder *et al.*[32] and curves showing our simulated result. The agreement between theory and experiment is quite good for both 100 Hz and 1 kHz. There is a discrepancy at 100 kHz. Our simulation predicts a much faster decay rate than that obtained from experiment. Despite this discrepancy, the qualitative trend of frequency dependence can be reproduced.

There are similar discussions on the role of the switching-cycle and frequency-dependent space charge density on the polarization fatigue in the literature. Dimos *et al.*[33] also suggested that polarization fatigue is a result of the imbalance between the charge trapping and detrapping rates. The number of charged vacancies increases after repeated switching cycles if the first rate is larger than the second one. Dawber *et al.*[34] have obtained a similar result. The switched charge per unit area $P(N)$ decreases due to the electromigra-

tion of oxygen vacancies from the electrode/film interface. They suggested that $P(N)$ is inversely proportional to the concentration of oxygen vacancies. However, they did not explain how this relation was derived. Majumder *et al.*[32] have obtained a similar fitted relation from the experimental result. For comparison, we have derived the switching cycle and frequency-dependent space charge density from the imbalance of trapping and detrapping rates from oxygen vacancies.

The coercive field may also change with switching cycles. There is still no unequivocal conclusion on how it changes. From some experiments[12,24] with samples using a metal electrode, it was found that the coercive field increased with switching cycles, as what we can expect from our present result. The opposite result has also been reported with samples using an oxide electrode.[35] We suggested that, in addition to oxygen vacancy, there are many other species responsible for polarization fatigue, resulting in different effects on the coercive field. Ricinschi *et al.*[30] have observed the decrease in the coercive field after 10^7 switching cycles in sol-gel PZT thin film, but an increase in the sputtered PZT thin film. They suggested that the major cause for fatigue in sol-gel film is space charge accumulation, but that in sputtered film is due to mobile charged defects. Consequently, the mobility of charged defects plays an important role in the enhancement of a coercive field. The experimental result performed by Majumder *et al.*[32] also supports this conclusion. They observed the increase in the coercive field in an undoped PZT film, but a decrease in a cerium-doped film after a number of switching cycles. The size of the Ce^{4+} ion is larger than those of Ti^{4+} and Zr^{4+} ions. When cerium is doped into the PZT film, the empty space within the lattice is reduced. The mobility of oxygen vacancies is then reduced. Consequently, oxygen vacancies cannot reach the interior region of the film. On the other hand, an explanation on the reduction of a coercive field during the polarization fatigue is rare, even though it has been observed in some experiments.[30,32,35] This demands further investigation.

IV. CONCLUSION

The role of oxygen vacancies in a ferroelectric thin film has been investigated. A numerical simulation on thickness dependence and polarization fatigue has been performed using a two-dimensional four-state Potts model. The switching of the dipole by displacing a Ti^{4+} ion from one equilibrium site to the other is influenced by the presence of an oxygen vacancy in the perovskite cell. Moreover, the distributed oxygen vacancies induces thickness dependence of the coercive field and remanent polarization. On the other hand, oxygen vacancy induces a frequency-dependent space charge distribution due to the imbalance in the trapping and detrapping rates of holes. The accumulation in space charge results in the screening of an external electric field, leading to polarization fatigue. The coercive field is simultaneously enhanced. The experimental thickness dependence of the coercive field and remanent polarization, as well as temperature, amplitude of the driving voltage and frequency polarization fatigue have been reproduced by a numerical simulation.
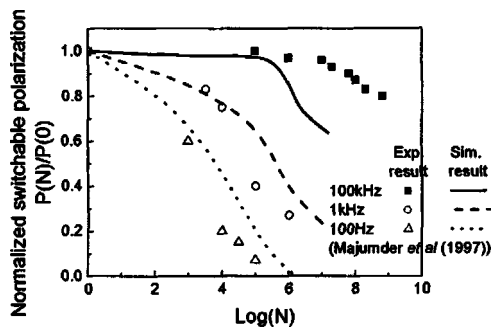

FIG. 10. The effect of frequency on polarization fatigue: curves: simulated result; symbols: experimental result from Majumder *et al.* (see Ref. 32).

ACKNOWLEDGMENTS

[1] J. F. Scott, *Ferroelectric Memories* (Springer-Verlag, Berlin, 2000).

[2] K. R. Udayakumar, P. J. Schuele, J. Chen, S. B. Krupanidhi, and L. E. Cross, J. Appl. Phys. **77**, 3981 (1995).

[3] J. Zhu, X. Zhang, Y. Zhu and S. B. Desu, J. Appl. Phys. **83**, 1610 (1998).

[4] A. K. Taganstev and I. A. Stolichnov, Appl. Phys. Lett. **74**, 1326 (1999).

[5] P. K. Larsen, G. J. M. Dormans, D. J. Taylor, and P. J. van Veldhoven, J. Appl. Phys. **76**, 2405 (1994).

[6] H. Z. Jin and J. Zhu, J. Appl. Phys. **92**, 4594 (2002).

[7] L. J. Sinnamon, R. M. Bowman, and J. M. Gregg, Appl. Phys. Lett. **78**, 1724 (2001).

[8] V. M. Fridkin, S. Ducharme, A. V. Bune, S. P. Palto, S. G. Yudin, and L. M. Blinov, Ferroelectrics **236**, 1 (2000).

[9] K. T. Li and V. C. Lo, J. Ceram. Soc. Jpn. **112**, S1 (2004).

[10] W. Ma, M. Zhang, L. Sun, Y. Chen, N. Ming, Y. Jin, and Q. Huang, Ferroelectr., Lett. Sect. **23**, 153 (1998).

[11] A. K. Tagantsev, I. Stolichnov, E. L. Colla, and N. Setter, J. Appl. Phys. **90**, 1387 (2001).

[12] W. L. Warren, D. Dimos, B. A. Tuttle, G. E. Pike, R. W. Schwartz, P. J. Clews, and D. C. Mclntyre, J. Appl. Phys. **77**, 6695 (1995).

[13] A. Q. Jiang, J. F. Scott, and M. Dawber, J. Appl. Phys. **92**, 6765 (2002).

[14] H. M. Duiker, P. D. Beal, J. F. Scott, C. A. Pas de Araujo, B. M. Melnice, J. D. Cuchiro, and L. D. McMillan, J. Appl. Phys. **68**, 5783 (1990).

[15] C. H. Park and D. J. Chadi, Phys. Rev. B **57**, R13961 (1998).

[16] C. W. Law, K. Y. Tong, J. H. Li, and M. C. Poon, Thin Solid Films **354**, 162 (1999).

[17] J. F. Scott, C. A. Paz de Araujo, B. N. Melnick, L. D. McMillan, and R. Zuleeg, J. Appl. Phys. **70**, 382 (1991).

[18] L. He and D. Vanderbilt, Phys. Rev. B **68**, 134103 (2003).

[19] V. Nagarajan, I. G. Jenkins, S. P. Alpay, H. Li, S. Aggarwal, L. Salamanca-Riba, A. L. Roytburd, and R. Ramesh, J. Appl. Phys. **86**, 595 (1999).

[20] H. Qian and L. A. Bursill, Int. J. Mod. Phys. B **10**, 2027 (1996).

[21] S. Tsunekawa, T. Fukuda, T. Ozaki, Y. Yoneda, T. Olabe, and H. Terauchi, J. Appl. Phys. **84**, 999 (1998).

[22] F. Y. Wu, Rev. Mod. Phys. **54**, 235 (1982).

[23] V. C. Lo, J. Appl. Phys. **92**, 6778 (2002).

[24] V. C. Lo, K. H. Wong, and K. S. So, Thin Solid Films (to be published).

[25] S. M. Sze, *Physics of Semiconductor Devices*, 2nd ed. (Wiley, New York, 1981).

[26] T. Mihara, H. Watanabe, and C. A. Pas de Araujo, Jpn. J. Appl. Phys., Part 1 **33**, 5281 (1994).

[27] S. W. Sides, P. A. Rikvold, and M. A. Novotny, Phys. Rev. E **59**, 2710 (1999).

[28] F. Joan and G. Shirane, *Ferroelectric Crystals* (Pergamon, New York, 1993).

[29] H. Fujisawa, S. Nakashima, K. K. M. Shimizu, and H. Niu, Jpn. J. Appl. Phys., Part 1 **38**, 5392 (1999).

[30] D. Ricinschi and M. Okuyama, Integr. Ferroelectr. **50**, 149 (2002).

[31] E. Paton, M. Brazier, S. Mansour, and A. Bement, Integr. Ferroelectr. **18**, 29 (1997).

[32] S. B. Majumder, Y. N. Mohapatra, and D. C. Agrwal, Appl. Phys. Lett. **70**, 138 (1997).

[33] D. Dimos, H. N. Al-Shareef, W. L. Warren, and B. A. Tuttle, J. Appl. Phys. **80**, 1682 (1996).

[34] M. Dawber and J. F. Scott, Appl. Phys. Lett. **76**, 1060 (2000).

[35] H. N. Al-Shareef, B. A. Tuttle, W. L. Warren, T. J. Headley, D. Dimos, J. A. Voigt, and R. D. Nasby, J. Appl. Phys. **79**, 1013 (1996).